

## APPENDIX C: THE EFFECT OF DEFECTS

The current research demonstrated an approach using beam and shell elements for simulating the reorientation of fabric yarns due to the fabric mechanical behavior and manufacturing process conditions such as interlaminar friction. This simulation is capable of locating problematic areas for forming and the potential forming of defects that can compromise the in-service performance of the blade. Ideally, it would be beneficial if the finite element model resulting from the manufacturing process, where the final yarn orientations and local stiffnesses are known, could be used to conduct in-service structural performance analyses of the blade. Such a model would seamlessly account for the influence of these defects on the local state of stress in the region of defect and the overall stiffness of the blade.

The wave defect sizes selected and embedded in the actual CX-100 spar cap were likewise embedded in the spar cap of the blade model and the strain field was analyzed. This appendix summarizes the use of the finite element method to study analytically how the size and location of wave defects impact the effective strain amplification.

Forming simulations showed that the yarns in the root layers of the CX-100 did not significantly shear relative to one another, but these yarns did develop some in-plane waviness. It is well known that even small changes in fiber orientation in a composite material can significantly affect stiffness and strength. While both the beam/shell and orthotropic shell structural modeling approaches can capture stiffness changes due to uniform shearing of a fabric, only the beam/shell approach can capture stiffness changes due to nonuniform shearing by discretely modeling the direction of the yarns. The

orthotropic shell approach assumes that the yarns remain orthogonal even as they rotate, thereby requiring the use of knockdown factors to simulate the structural stiffness of the laminate properly.

### **1 Advantage of the Beam/Shell Structural Modeling Approach**

To demonstrate the advantage of the beam/shell structural modeling approach, a formed layer in the LP root section of the blade (0.5-m long) was cantilevered, and a tip deflection of 25.4 mm was prescribed (Figure C-1). The load required to achieve the 25.4-mm displacement was compared between a beam/shell model and an orthotropic shell model of the same layer using the properties in Table C-1 and Table C-2, respectively. As shown in Table C-3, without the use of knockdown factors to account for nonuniform shearing, the orthotropic shell model overpredicts the stiffness of the layer by 130% when compared to the beam/shell model. This overprediction can lead to a lack of confidence in the orthotropic shell model and potentially force designers to add layers of fabric in the root section to ensure that the root will be structurally sound. As a consequence, the weight and cost of the blade unnecessarily increase.

**Table C-1. E-LT 5500 cured beam/shell properties**

<b>Section Property</b>	<b>0° yarns</b>	<b>90° yarns</b>
<b>beam E (GPa)</b>	60.58	60.58
<b>beam <math>\nu</math></b>	0.22	0.22
<b>shell E (GPa)</b>	2.95	2.95
<b>shell <math>\nu</math></b>	0.30	0.30
<b>beam A (mm<sup>2</sup>)</b>	2.37	0.22
<b>beam I<sub>11</sub> (mm<sup>4</sup>)</b>	0.286	0.171
<b>beam I<sub>12</sub> (mm<sup>4</sup>)</b>	0	0
<b>beam I<sub>22</sub> (mm<sup>4</sup>)</b>	0.700	0.000087
<b>beam J (mm<sup>4</sup>)</b>	0.812	0.000347
<b>shell thickness, t (mm)</b>	0.571	

**Table C-2. Orthotropic shell lamina properties derived from unit-cell model**

<b>Property</b>	<b>Value</b>
<b>E<sub>0°</sub> (GPa)</b>	45.0
<b>E<sub>90°</sub> (GPa)</b>	18.0
<b>G<sub>0/90</sub> (GPa)</b>	6.1
<b><math>\nu</math></b>	0.256
<b>density, <math>\rho</math> (kg/m<sup>3</sup>)</b>	1,823.0
<b>shell thickness (mm)</b>	1.2

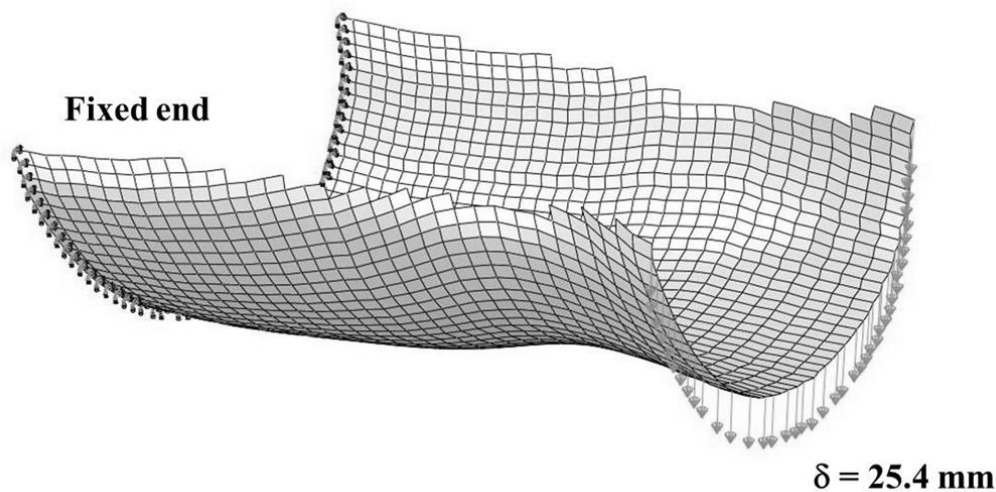


**Figure C-1. Boundary conditions applied to beam/shell and orthotropic shell root fabric layer**

**Table C-3. Comparison of tip loads in root layer between beam/shell and orthotropic shell approaches**

	<b>Beam/Shell</b>	<b>Orthotropic Shell</b>	<b>% Difference</b>
<b>Tip Load (N)</b>	1076	2478	130%

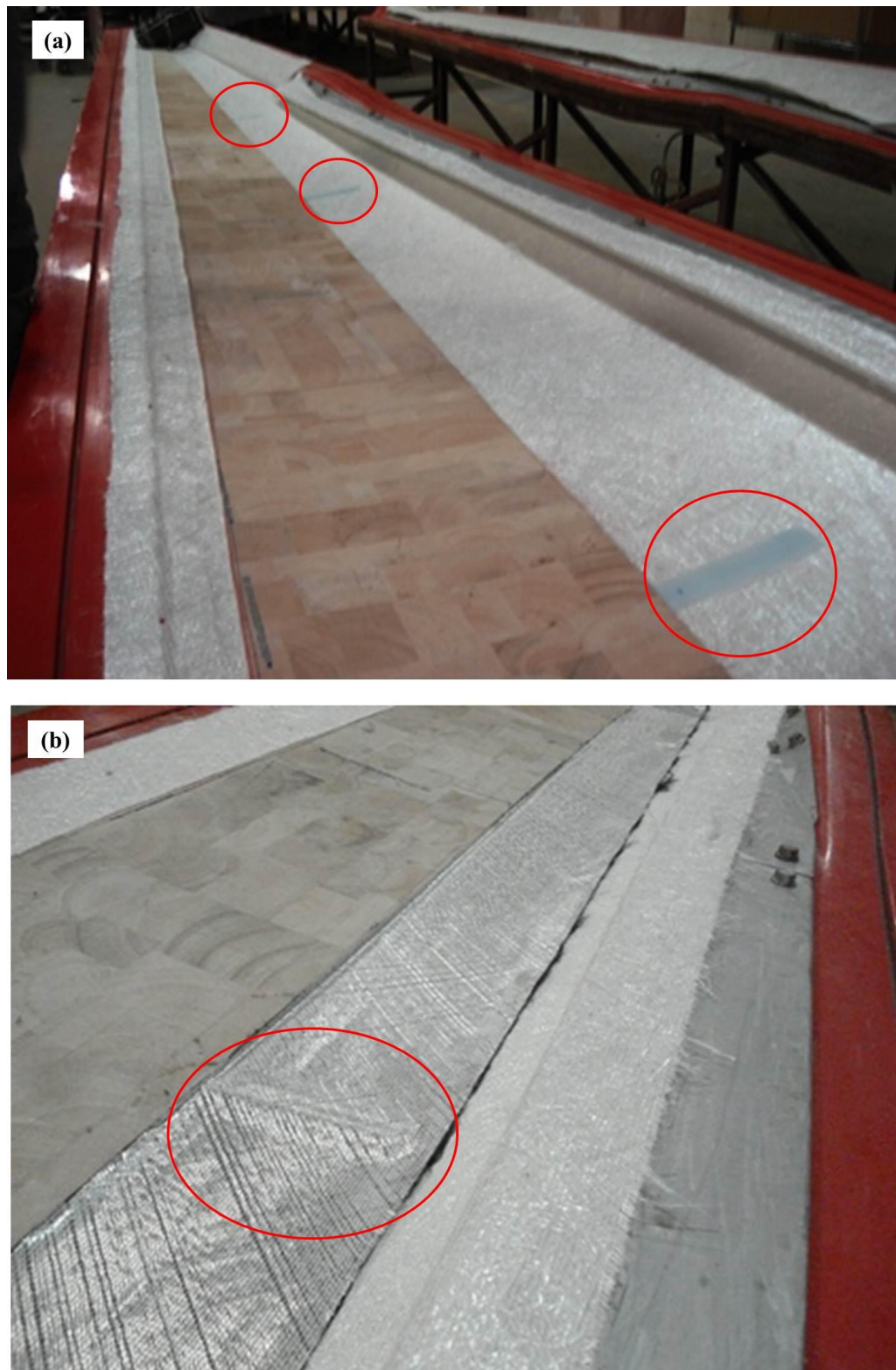
## 2 Presence of Wave Defects

Table C-4 summarizes the defect sizes and locations along the blade length. The justification for these choices of defect lengths and aspect ratios was based on experience from what length and aspect ratios are typically found in blades per the input from our collaborators at TPI Composites (Steve Nolet) and Sandia National Labs (Mark Rumsey). The defects were laid on top of the two layers of double-bias fabric (Figure C-2a) that sit over the gelcoat layer, and beneath the first fabric layer of the spar cap (Figure C-2b). The location of these defects corresponds to what was classified as an “A-side” defect in

the coupon studies. Once manufactured, the blade was sent to the National Renewable Energy Laboratory (NREL) in Golden, Colorado for flexure and fatigue testing.

**Table C-4. Dimensions and locations of wave defects embedded in CX-100 spar cap**

<b>Defect amplitude (mm)</b>	<b>Defect aspect ratio (Length/Amplitude)</b>	<b>Distance from blade root (m)</b>
3	5	6.0
3	10	5.0
3	15	3.5



**Figure C-2. Insertion of wave defects (a) on top of double-bias layers and (b) beneath the first spar-cap layer in CX-100**

For the flexure testing at NREL, a 2.3-kN weight was hung from the 6.75-m location to deflect the cantilevered blade statically. A digital image correlation (DIC) system was used to measure the strain on the surface of the blade and to capture and quantify the amplification of strain at the defect locations, similar to those measurements made on coupon specimens [1]. While those measurements are part of a separate study in which the analysis of the measurements was ongoing at the time of this research, Figure C-3 shows an example of a DIC measurement at the 5.0-m location along the LP side of the CX-100. The strain across the surface of the blade as indicated by the double-arrow line in Figure C-3 is plotted in Figure C-4 where the nominal strain away from the defect is compared to the magnitude of the amplified strain at the location of the defect.

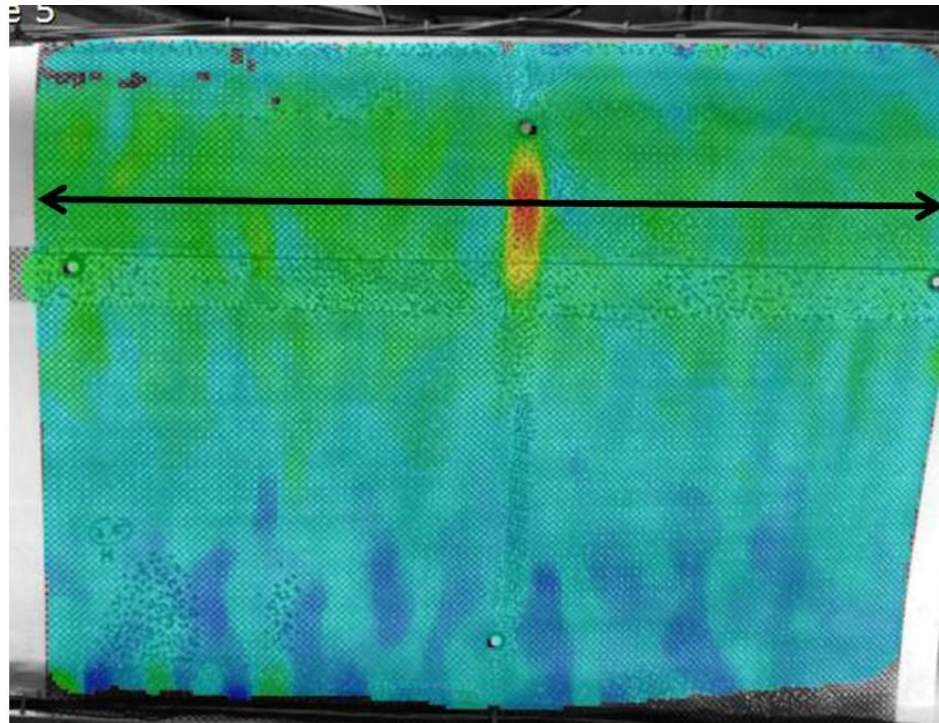


**Figure C-3. DIC measurement of strain at the 5.0-m location along the LP side of a CX-100 blade**

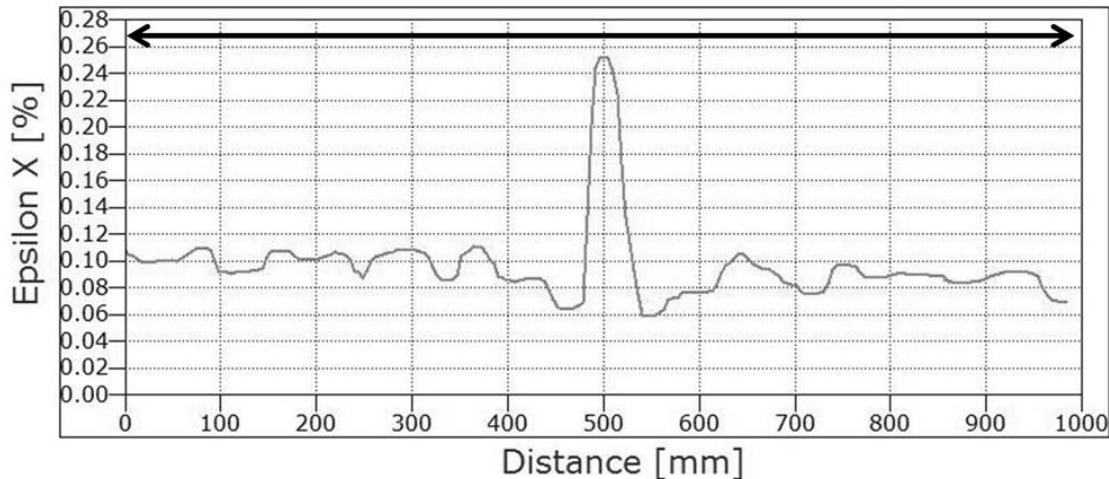


**Figure C-4. DIC strain measurements along a line of interest passing through the location of a defect**

Similar defects as were placed in the blade manufactured at TPI composites were embedded at the same axial locations (3.5, 5.0 and 6.0 m) along the LP spar cap of the finite element model of the CX-100 blade (Figure C-5). The model was loaded at the 6.75-m location with a 2.3-kN weight, as done in the lab test of the blade. Note that the beam/shell approach was used for this model, and the structural properties assigned to all of the NCFs were equal to those of the E-LT 5500 because that was the only fabric that had been tested as a cured laminate at this point in research timeline. The model does capture the strain amplification in the immediate regions surrounding the wave defects. The strain contours in Figure C-6 can be used to show qualitatively the magnitude of the amplification of strain in the regions of the three defect locations relative to the defect-free regions.

Consider a case in which the defect locations were unknown. Without a model such as the beam/shell model in this research capable of capturing out-of-plane deformation as a result of the material behavior and/or processing parameters, the

resulting structural model would never capture the amplification of strain and the blade may be considered to be structurally sound.

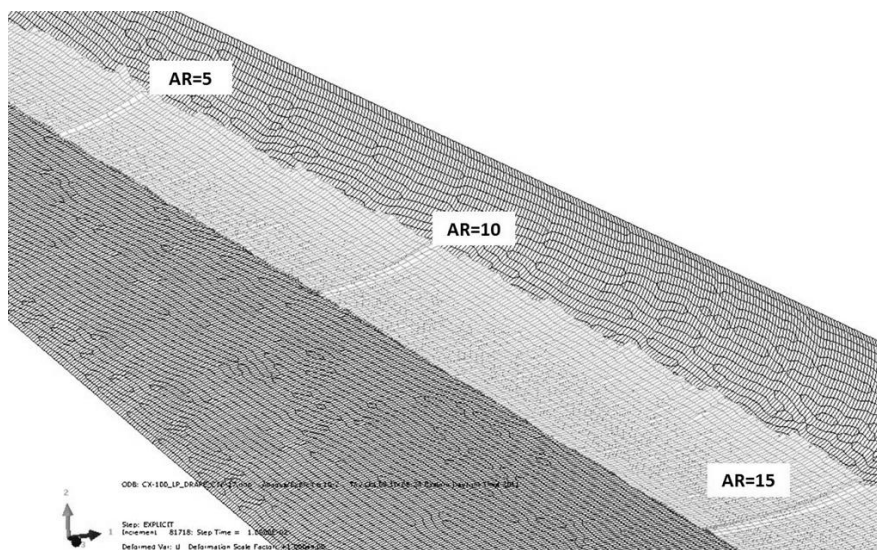


**Figure C-5. Spar-cap layers laid over wave defects in CX-100 finite element model**



**Figure C-6. Amplification of strain on LP side of CX-100 FE model at three defect locations**

As was done with DIC measurements in Figure C-4, a double-arrow line of interest can be drawn across the LP surface of the finite element model of the blade (Figure C-7) to compare the magnitude of the nominal strain away from the defect to the magnitude of the amplified strain at the location of the defect (Figure C-8). Thus, the finite element model can be used to investigate the effect of defects on the structural integrity of wind turbine blades rather than having to set up expensive test equipment and manufacturing an actual blade with defects.

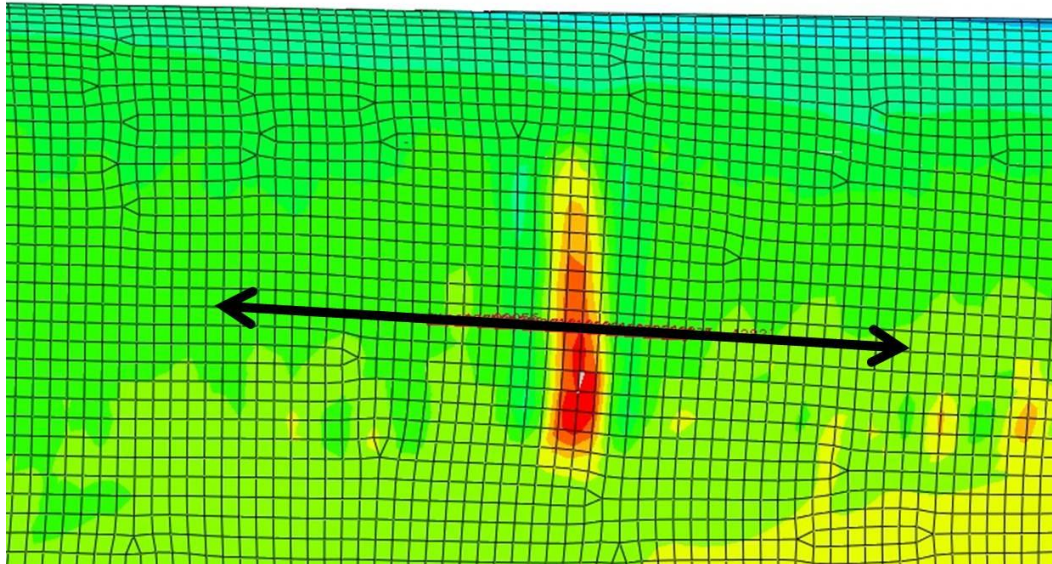


**Figure C-7. Line of interest across the LP blade surface to comparing nominal and amplified strain at defect location**

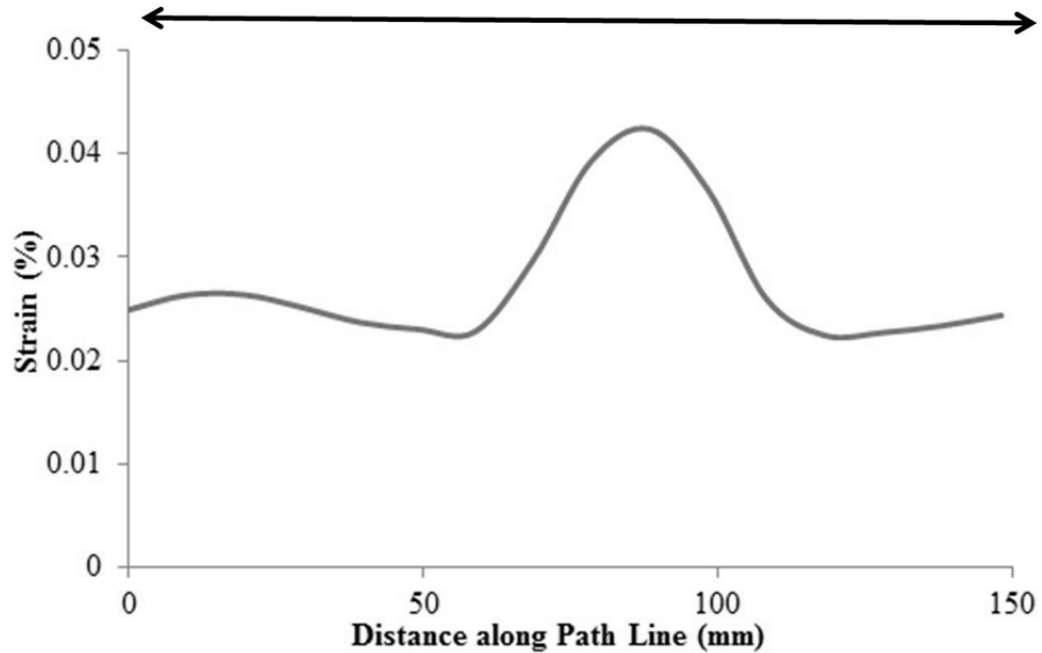


**Figure C-8. Strain along the line of interest drawn in the finite element model of the blade at the location of a wave defect**

### 3 Wave defect scalability

In some instances during the manufacturing process, a defect may form in a location that is not critical to the overall health of the blade. Oftentimes, these defects have to form as a consequence of the fabric conforming to the shape of the mold, and the finite element method can give insight as to how the blade can be manufactured in a way that pushes those defects to one or more noncritical locations [2]. However, if that same defect had been located in another area of the blade, it could lead to a catastrophic failure. Because it is not practical to test an infinite number of combinations of wave sizes and locations, the finite element model can be used to indicate whether or not the relationship between wave-defect sizes, locations and compressive strength is scalable over various section thicknesses. In this research, the defect amplitudes,  $h$ , are normalized by the coupon thickness,  $t_c$ , according to Figure C-9, and the reduction in the compressive load

is investigated. The load knockdown factor is also explored as a function of through-thickness location ( $b/t_c$ ). The model parameters are summarized in Table C-5.

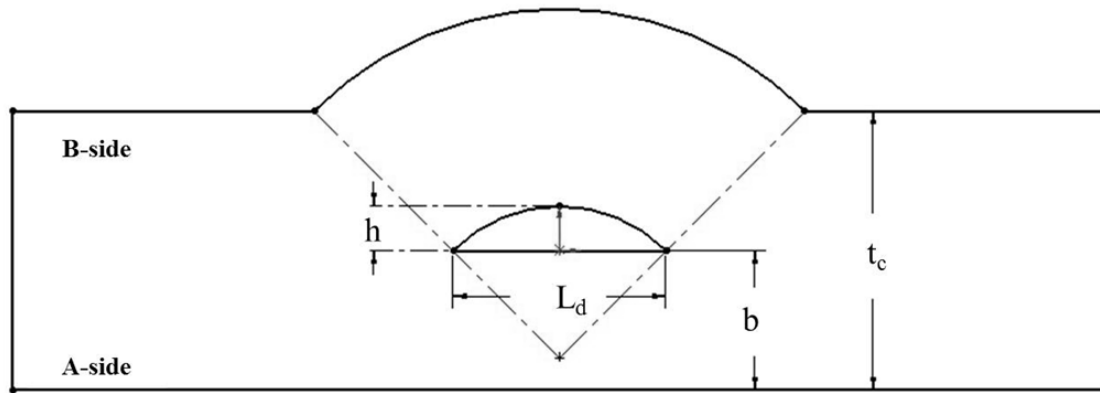


**Figure C-9. Wave defect parameters in a composite coupon specimen**

**Table C-5. Parameters studied with FE compression coupon models**

Model No.	wave height, h (mm)	$h/t_c$	aspect ratio, $L_d/h$	location, $b/t_c$
1	3	0.26	10	0.75 (B-side)
2	1	0.09		0.50 (Middle)
3	2	0.17		
4	3	0.26		
5	3	0.26		0.25 (A-side)

Figure C-10 is a plot of the load knockdown factors from each of the five models cited in Table C-5. As the wave defect occupies more of the sample thickness, i.e. as  $h/t_c$  increases, the compressive load-carrying capacity of the coupon decreases. Also, the decrease in compressive load as the defect moves closer to the A-side of the sample correlates to the trend observed in the testing of the wave-defect coupons, where it was concluded that the load carrying capacity increases as the location of the defect moves from the A side to the B side.

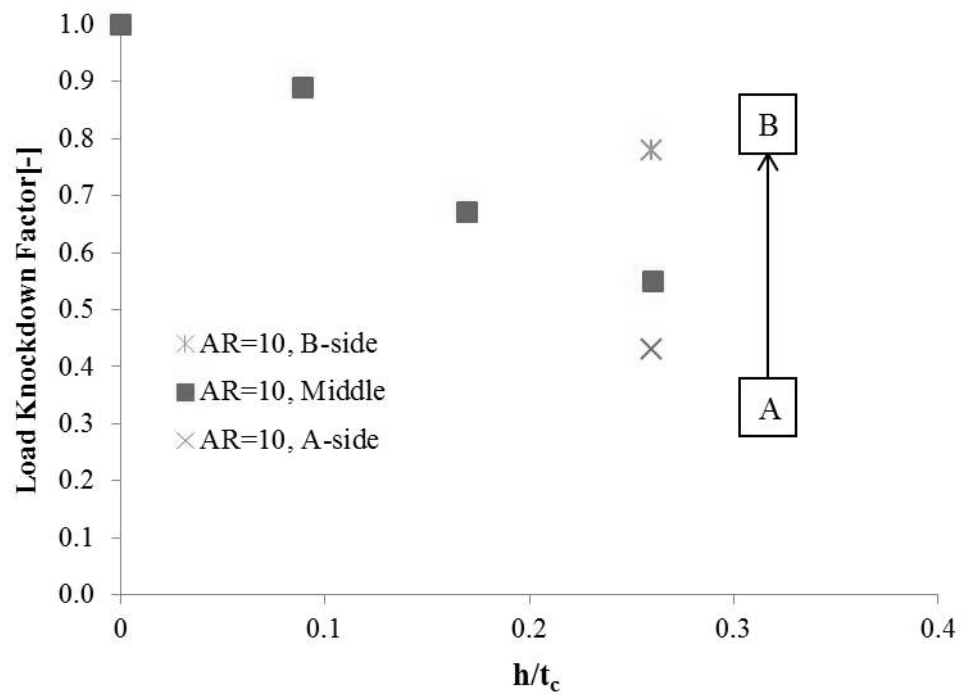


**Figure C-10. Compressive load knockdown factor as a function of  $h/t_c$**

To study the scalability of the effects seen in Figure C-10, additional coupon models were generated with half the thickness (5 mm) of the models that were compared to test coupons. Wave defect dimensions were chosen such that the  $h/t_c$  and  $b/t_c$  ratios remained equal to those previously studied. Additional  $b/t_c$  ratios were studied, as shown in Table C-6. Figure C-11 shows the resulting compressive load knockdown factors with linear lines fit through the data points to show general trends. The plot shows that the effect of defects on compressive strength is scalable if the wave dimensions are related to the section thickness. This approach can potentially be used to investigate what effect a defect will have if located in a region of a wind turbine blade with a certain thickness.

**Table C-6. Additional coupon model parameters studied**

Model #	wave height, h (mm)	$h/t_c$	aspect ratio, $L_d/h$	location, $b/t_c$
1	0.60	0.09	10	0.75 (B-side)
2	1.14	0.17		
3	1.75	0.26		
4	0.60	0.09		0.50 (Middle)
5	1.14	0.17		
6	1.75	0.26		
7	0.60	0.09		0.25 (A-side)
8	1.14	0.17		
9	1.75	0.26		

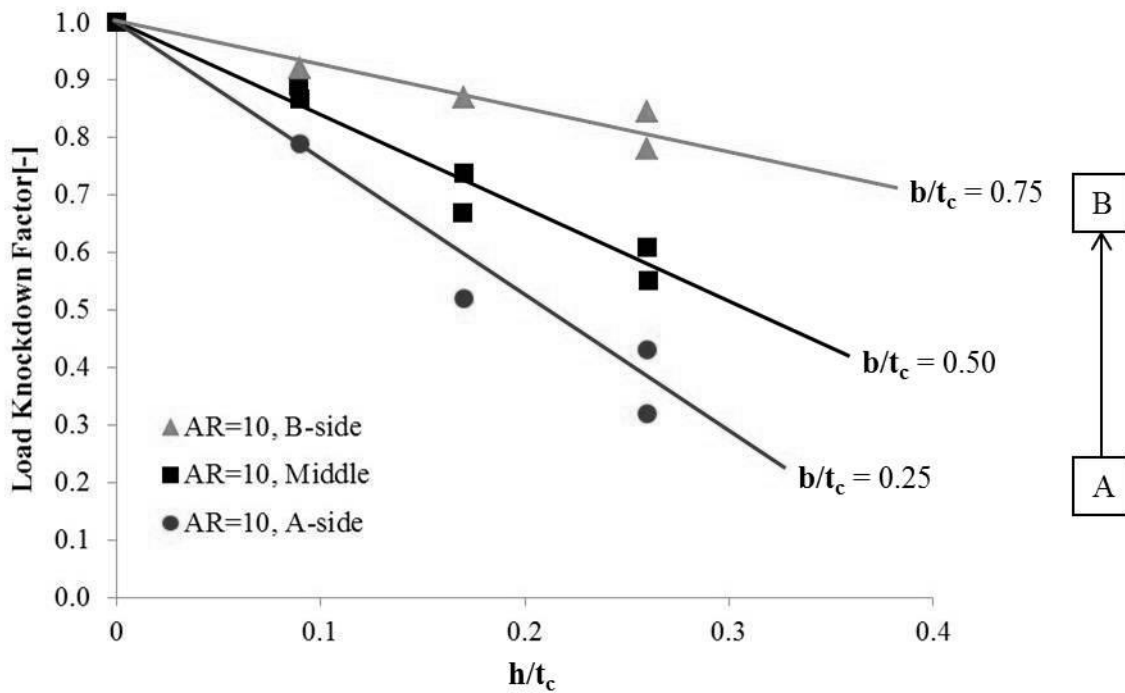


**Figure C-11. Load knockdown factor as a function of  $h/t_c$  and  $b/t_c$**

**SUMMARY**

Wave defects with controlled dimensions were embedded in three different locations along the spar cap of a CX-100 blade model. The blade was fixed at the root and loaded at the 6.75-m location with a 2.3-kN weight. Despite using only the structural properties of an E-LT 5500 laminate, the finite element model showed the amplification of strain at the location of the three defects. This amplified strain was similar to typical measurements made using a digital image correlation system.

**LITERATURE CITED**

- [1] LeBlanc, B.: “Non-destructive Inspection of Wind Turbine Blades with Three Dimensional Digital Image Correlation”, Master’s Thesis, Dept. of Mechanical Engineering, University of Massachusetts Lowell, 2011.
  
- [2] Frank, M.  
Iowa State University  
Blade Manufacturing Panel Session Discussion, 2011 Wind Energy Research Workshop, University of Massachusetts Lowell, September 22-23, 2011.